PARTICLE ACCELERATION AND TRANSPORT DURING 3D CME ERUPTIONS

Qian Xia,[1] Joel T. Dahlin,[2, *] Valentina Zharkova,[1] and Spiro K. Antiochos[3]

[1] Department of Mathematics, Physics and Electrical Engineering
Northumbria University, UK
[2] NASA Goddard Space Flight Center, Greenbelt, Maryland 20771
[3] NASA Goddard Space Flight Center, Greenbelt, Maryland 20771, USA

ABSTRACT

We calculate particle acceleration during corona mass ejection (CME) eruptions using combined magnetohydrodynamic (MHD) and test-particle models. The 2.5D/3D CMEs are generated via the breakout mechanism. In this scenario a reconnection at the "breakout" current sheet (CS) above the flux rope initiates the CME eruption by destabilizing a quasi-static force balance. Reconnection at the flare CS below the erupting flux rope drives the fast acceleration of the CME, which forms flare loops below and produces the energetic particles observed in flares. For test-particle simulations, two times are selected during the impulsive and decay phases of the eruption. Particles are revealed to be accelerated more efficiently in the flare CS rather than in the breakout CS even in the presence of large magnetic islands. Particles are first accelerated in the CSs (with or without magnetic islands) by the reconnection electric field mainly through particle curvature drift. We find, as expected, that accelerated particles precipitate into the chromosphere, or become trapped in the loop top by magnetic mirrors, or escape to interplanetary space along open field lines. Some trapped particles are reaccelerated, either via reinjection to the flare CS or through a local Betatron-type acceleration associated with compression of the magnetic field. The energetic particles produce relatively hard energy spectra during the impulsive phase. During the gradual phase, the relaxation of magnetic field shear reduces the guiding field in the flare CS, which leads to a decrease in particle energization efficiency. Important implications of our results for observations of particle acceleration in the solar coronal jets are also discussed.

Keywords: Plasmas – Acceleration of particles – Sun: flares – Sun: coronal mass ejections (CMEs) –
Magnetic reconnection

Corresponding author: Q. Xia
q.xia@northumbria.ac.uk

* NASA Postdoctoral Program Fellow

1. INTRODUCTION

Corona mass ejections (CMEs) are explosive solar events that involve enormous ejections of plasma and magnetic flux and drive interplanetary dynamics (Gosling 1993, 1994). CMEs are always associated with a filament channel, in the form of a twisted flux rope or sheared arcade, that stores the required free magnetic energy to power the eruption (Gaizauskas 1998; Martin 1998). These structures erupt when destabilized either by reconnection (Antiochos et al. 1999; Moore et al. 2001) or an ideal process, e.g. the torus or kink instability (Amari et al. 2000; Forbes et al. 2006; Titov et al. 2008; Wyper et al. 2017). These eruptions are often accompanied by multiribbon flares and solar energetic particles.

In the *magnetic breakout* model (Antiochos et al. 1994), the energy buildup in the filament channel deforms a coronal nullpoint external to the system to form a current sheet (CS). This CS (breakout CS) eventually reconnects, removing the flux overlaying the filament channel, disrupting the force balance, and triggering eruption onset (Antiochos 1998; DeVore & Antiochos 2008; Karpen et al. 2012). A vertical CS (flare CS) forms beneath the erupting filament and reconnects and drives explosive CME acceleration (Antiochos et al. 1999; Karpen et al. 2012). Plasma heated at the flare CS is transferred to post-flare loops, producing flare brightening as well as soft and hard X-ray emission (Gosling 1993; Hudson et al. 1995; Kay et al. 2003; Zharkova et al. 2011). It should be emphasized that the vertical flare CS is a generic feature of all CME models, including those that are initiated by a kink or torus instability (e.g. Fan 2010).

Observations of flares show that a significant fraction of the total released magnetic energy is transferred to high-energy electrons and ions (Lin & Hudson 1976; Miller et al. 1997; Lin & Team 2003; Emslie et al. 2005; Vilmer et al. 2011; Emslie et al. 2012). Energetic electrons in flares are observed through bremsstrahlung hard X-ray and gyrosynchrotron microwave emission from the solar corona and chromosphere. There are clear indications of strong particle energization during solar flares (Holman et al. 2011; Vilmer et al. 2011; Zharkova et al. 2011), which may be driven by various mechanisms associated with the magnetic reconnection process producing the energy release (Priest & Forbes 2000; Somov & Oreshina 2000; Zharkova et al. 2011). At the same time, a fraction of energetic particles is shown to escape to interplanetary space as solar energetic particles that can be detected by in-situ observations. By studying particle energization in different breakout and flare CSs occurring during a CME evolution we aim to understand the energy release by magnetic field restructuring in these events and the energy transfer to energetic particles, and thus determine the properties of the high energy particles produced.

Particle acceleration in the complex magnetic structures of a CME could be associated with various reconnection CSs, which may contain single or multiple X-nullpoints and O-nullpoints, or magnetic islands (Drake et al. 2006; Daughton et al. 2011). The combination of MHD and test-particle methods have been implemented to explore various particle energization mechanisms, such as super-Dreicer electric field, resistive electric field, turbulence, and collapsing magnetic traps, etc. (see, for example, Gordovskyy & Browning 2012; Grady et al. 2012; Vilmer 2012; Birn et al. 2017; Borissov, A. et al. 2017; Isliker et al. 2019, and references therein). Nevertheless, the simulations were targeted on a single specific process and restricted to the limited regions of interests.

Particle acceleration in these magnetic configurations was previously evaluated by a number of authors who considered electric currents formed by anomalous resistivity in MHD reconnection simulations. The corresponding resistive electric fields were found to range from $0.1 - 0.6 V m^{-1}$ (Zhou et al. 2016), or even higher (Turkmani et al. 2006; Gordovskyy et al. 2010a,b). This is orders of magnitude lower than the inductive electric field by the plasma motion and restricted to the diffusion layers around the X-nullpoints, and would hence only accelerate a few particles.

However, the inductive electric field induced by plasma flows perpendicular to the CS plane can efficiently accelerate the particles over a larger region and set up the conditions for further acceleration by the generated turbulence, etc (Zharkova & Gordovskyy 2004; Zharkova & Agapitov 2009; Dahlin et al. 2014; Guo et al. 2014). These conclusions are supported by various transport models developed to describe macro-scale particle acceleration (Zank et al. 2014; le Roux et al. 2015; Li et al. 2018; Drake et al. 2019). These studies show that kinetic-scale layers may not be essential for the study of particle energization in macroscopic systems. Since CME structures are much larger than the typical ($\sim$ meter) kinetic scales in the corona, our test-particle approach focuses on mechanisms operating on these macro-scales.

In this paper, we investigate particle energization and transport during a large CME by directly simulating the orbits of test particles in an MHD simulation. We examine both the impulsive and gradual phase of flare reconnection in an ultra-high resolution 2.5D MHD simulation (Karpen et al. 2012), for which the main differences

between the two phases are the decaying strength of the reconnection guide field and the slackening of the reconnection rate. The guide field decrease is associated with a reduction in shear of post-flare loops (Fletcher et al. 2011). Particle acceleration results obtained for 2.5D MHD models with plasmoids in the breakout sheet are compared with those for a 3D MHD simulation, in which plasmoids are generated in the flare CS instead. This paper is organized as follows: the simulation methods and units are briefly described in section 2. The simulation results are analyzed in section 3, and the conclusions are drawn in section 4.

2. MHD/TEST-PARTICLE APPROACH AT LARGE CME SCALE

2.1. *Formulation of the problem*

In this paper, we study particle acceleration processes by integrating the particle motion equations using the output from the ideal MHD simulation code ARMS (DeVore & Antiochos 2008). We focus on ultra-high resolution, adaptively refined 2.5D simulations following the configuration described in Karpen et al. (2012), but also examine a 3D simulation that was described in Dahlin et al. (2019). Our 2.5D simulations use nine levels of adaptive refinement to selectively resolve fine-scale structure (as compared to six in Karpen et al. (2012)). Both simulations represent idealized eruption configurations, so we apply rescaling factors to the MHD data before simulating particle motions. We adopt the following parameters typical for large eruptive flares: coronal magnetic field $10-100$ G, CS length 10^3 km, and electric field $E \leq 1000 V m^{-1}$.

2.2. *ARMS MHD simulations*

The one fluid MHD code ARMS solves the ideal MHD equations in spherical coordinates (DeVore & Antiochos 2008):

$$\frac{\partial \rho}{\partial t} + \nabla \cdot \rho \mathbf{V} = 0,$$
$$\frac{\partial \rho \mathbf{V}}{\partial t} + \nabla \cdot \rho \mathbf{V V} = -\nabla \mathbf{P} + \frac{1}{4\pi}(\nabla \times \mathbf{B}) \times \mathbf{B} + \rho g,$$
$$\frac{\partial T}{\partial t} + \nabla \cdot T \mathbf{V} = (2 - \gamma)T\nabla \cdot \mathbf{V},$$
$$\frac{\partial \mathbf{B}}{\partial t} - \nabla \times (\mathbf{V} \times \mathbf{B}) = 0 \tag{1}$$

where ρ is the mass density, $\mathbf{V}$ is the fluid velocity, $\mathbf{P}$ is the thermal pressure, g is gravity, T is the temperature, $\mathbf{B}$ is the magnetic field, and $\gamma = 5/3$ for the adiabatic process. The gravity of the Sun $g = -GM_s\mathbf{r}/r^3$, where G is the universal gravitational constant and M_s is the solar mass. There is no explicit resistivity in Eq. (1),

and hence the electric field $\mathbf{E} = -\mathbf{V} \times \mathbf{B}$ so that our simulations do not include particle energization due to the parallel electric fields. Closed boundary conditions are applied at the inner radial boundary, which is at the solar surface ($1R_s$), while the outer boundary at $30R_s$ is open. The initial magnetic field combines a dipole magnetic field and octupole spherical harmonics. Free energy is injected into the system using flows imposed at the inner boundary (see Karpen et al. 2012; Dahlin et al. 2019, for more details).

For the test-particle simulations, we extract the electric field $\mathbf{E}$ and magnetic field $\mathbf{B}$ from the period corresponding to the eruption of the system. We use static electromagnetic fields because the particle acceleration and transport are much faster than the macroscopic evolution time of the eruption events in those selected cases (Karpen et al. 2012). We leave the study of fast temporal variation of the particle acceleration to future work.

2.3. *Particle motion equations*

The motion of a charged particle in an electromagnetic field $\vec{E}$ and $\vec{B}$ is given by the relativistic equations of motion:

$$\frac{d\vec{p}}{dt} = q(\mathbf{E} + \mathbf{v} \times \mathbf{B}), \tag{2}$$
$$\frac{d\vec{r}}{dt} = \frac{\vec{p}}{m\gamma}, \tag{3}$$

where $\mathbf{v}(= \vec{p}/m\gamma)$ and $\vec{r}$ are the particle velocity and position vectors, q and m are the charge and the rest mass of the particle, $\vec{p}$ is the momentum vector and γ is the corresponding Lorentz factor defined as $\gamma = 1/\sqrt{1 - v^2/c^2}$. The factor $\mathbf{E}$ and $\mathbf{B}$ fields at the particle location are interpolated from the spatial grids of ARMS with a triangular shape function (Hockney & Eastwood 1981).

In order to solve the equations of motion given above, we use the Boris rotation algorithm, which is a widely used second-order accurate leap-frog scheme (Boris 1970; Ripperda et al. 2018). The numerical timesteps Δt for protons and electrons are chosen to be much smaller than the corresponding gyroperiods: $\Delta t < 0.1(m/qB_0)$. For $B_0 = 10^{-4}$ T, for example, $\Delta t = 2 \times 10^{-9}$ s for electrons and $\Delta t = 4 \times 10^{-6}$ s for protons. The test particles are set to be protons for most simulations to speed up the computations and to reduce the scale separation between the Larmor radius of particles and MHD grid length.

The particles are initialized in the MHD simulation domain with a Maxwellian distribution corresponding to the typical coronal temperature, 2×10^6 K. Particle trajectories are computed up to the boundaries of the MHD

data domain, where they are considered to escape from the system. The final properties of escaping particles are recorded and included in the calculation of statistics such as ensemble energies and particle energy spectra. The test-particle simulations halt at $t = 1$ s, which is much smaller than the timescale associated with the global flare evolution, justifying our use of static MHD fields.

3. RESULTS

3.1. *Energy spectra*

We selected three distinct frames from the MHD simulations as background electromagnetic fields for the test-particle simulations (see Figure 1). These include the two main reconnection sites in the breakout model as well as cases with strong/weak guide fields and plasmoids in the flare CS. The first two cases represent, respectively, the impulsive and gradual phases of the same 2.5D CME simulation: (case 1) Figures 1(a) and 1(c) are snapshots of the breakout and flare CSs at the same time during the impulsive phase, during which the flare CS has a strong guide field; (case 2) Figures 1(e) and 1(g) are taken during the gradual phase, during which the flare CS has a weak guide field and there are several large plasmoids in the breakout CS. The last example, (case 3) Figure 1(i) is the flare CS during the impulsive phase from a 3D simulation. This case represents reconnection with a strong guide field and with several small magnetic islands near the primary X-point.

For every CS, 10^5 test particles were initialized in the green regions in the left column of Figure 1. At the conclusion of the simulations, we obtained the energy spectrum as shown in the right column of Figure 1, which included both the escaped particles and the ones still in the MHD domain. A comparison between Figures 1(b) and 1(d), and Figures 1(f) and 1(h) reveals that particle acceleration in the flare CS region is more efficient than in the breakout CS, with or without a significant guide field.

We further note that particles gain more energy in the impulsive phase CSs with a stronger guide field. The energy spectra show that the highest energy protons achieve 5×10^4 eV (Figure 1b) to 3×10^6 eV (Figure 1d) while the maximum energy is only near $6 \times 10^3 - 2 \times 10^4$ eV in Figures 1(f) and 1(h). Particle acceleration is much weaker in those CSs with a weak guide field, even when there are several X-nullpoints (Figure 1g) and magnetic islands (Figure 1e). In many kinetic simulations of magnetic reconnection, particles are strongly accelerated near the X-nullpoints, magnetic islands, etc., within a few hundreds of ion inertial length (Drake et al. 2005, 2006; Siversky & Zharkova 2009; Oka et al. 2010;

Egedal et al. 2012; Guo et al. 2014; Nalewajko et al. 2015). Kinetic scales are also required for nonadiabatic ion preheating mechanisms (e.g., Drake et al. 2009b,a; Knizhnik et al. 2011) that may be important for generating M/Q abundance enhancements in impulsive SEPs. However, our results indicate that breakout reconnection, even with plasmoids, and gradual phase flare reconnection are less effective at accelerating particles than impulsive phase flare reconnection.

3.2. *Acceleration regions and particle transport*

In this section, we present trajectories of several of the highest energy protons and identify typical acceleration sites along the paths shown in Figure 2:

(1) The magnetic X-nullpoint is shown in Figure 2a, which corresponds to the super high-energy particles ($> 10^8$ eV) in the energy spectrum (Figure 1d). We should note that this is due to the artificial symmetry of the 2.5D system. The particle orbit shows that it is trapped in the X-nullpoint-like magnetic island rather than following the Speiser-type orbit (Speiser 1965). To study the motion of a single particle at the exact X-nullpoint goes beyond the scope of this paper and, in any case, the particle would move along the guide field and eventually impact the chromosphere, which is a realistic 3D situation.

(2) The MHD-scale magnetic islands are presented in both the flare (Figures 2e, g, and i) and the breakout CSs (Figure 2c), and even below the flare CS (Figure 2a), where the particles are indeed trapped in the islands and accelerated. We note that the particles gain much less energy in the two largest islands (Figure 1e) than in the small ones. This is because acceleration rate scales inversely with the island radius (e.g., Dahlin et al. 2014).

(3) Another location for particle acceleration is in the helmet-like loop top beneath the flare CS (see Figures 2g and 2h). This corresponds to the scenario of a "collapsing magnetic trap" (Somov & Kosugi 1997; Karlický & Bárta 2006; Borissov et al. 2016). In contrast to other studies that used a reflecting boundary to reinject particles to the loop top (Birn et al. 2017), here the particles are trapped in this region (Figure 2g) due to magnetic mirroring in the flare loop and are considered to escape from the system if they reach the footpoints. We find that secondary acceleration in this region requires the particles to be preaccelerated in the flare CS (Karlický & Bárta 2007), for example in the magnetic island near 1.08 R_s in Figure 2(i). Particles initialized in this helmet-like region gain little energy and quickly escape to the footpoints. We also note that, as discussed in section 3.1, particle acceleration is weak during the gradual phase shown in Figure 1(g). This case would therefore

not be likely to produce an observable flare due to a lack of energetic particles (Andrews 2003).

These large-scale particle simulations shed new insight into the importance of 'magnetic mirrors': particles that were previously accelerated and ejected from the CS (Figures 2e and 2i) may return to the reconnecting CSs from the exhausts. Such particles may experience several reaccelerations in the RCS as shown in Figure 2(i). These two examples show how the particles can be reaccelerated even when they escape downstream, $\geq 10^5$ km away from the reconnection sites. We emphasize that this reinjection is not due to a numerical periodic boundary or stochastic turbulence.

3.3. *Energization mechanisms*

In this section, we link particle acceleration processes to the bulk plasma dynamics. We first adopt the standard guiding-center theory in order to diagnose different particle acceleration regions. In the low-β corona, the generation of high-energy particles typically results from impulsive phenomena, such as solar flares, that involve the rapid conversion of magnetic energy to kinetic energy. We hence examine the magnetic field energy release through fluid expansion and contraction under magnetic tension to better understand the processes occurring at the primary particle acceleration sites.

3.3.1. *Particle drift description*

To study the macroscopic particle acceleration, various models have been developed to connect particle drift motion to fluid motion (Drake et al. 2006; Zank et al. 2014), which can be described as fluid compression and shear energization, etc. (Montag et al. 2017; Li et al. 2018). In the guiding-center approximation, the energy change of the magnetized particles of the same species can be written as (Northrop 1966; Dahlin et al. 2014)

$$\frac{d\epsilon}{dt} = E_\parallel J_\parallel + \frac{P_\perp}{B}\left(\frac{\partial B}{\partial t} + \mathbf{V}_E \cdot \nabla B\right) + \frac{P_\parallel}{B}\left(\mathbf{V}_E \cdot \kappa B\right) \quad (4)$$

where ϵ is the total kinetic energy, $E_\parallel$ and $J_\parallel$ are the parallel electric field and current, $\mathbf{V}_E = c\mathbf{E} \times \mathbf{B}/B^2$, the curvature $\kappa = \mathbf{b} \cdot \nabla \mathbf{b}$ with $\mathbf{b}$ as the unit vector along $\mathbf{B}$, and $P_\perp$, $P_\parallel$ are the parallel and perpendicular pressures. The first term on the right-hand side (RHS) can be ignored because $E_\parallel = 0$ in the model as mentioned in section 2.2. The second term corresponds to Betatron acceleration and the third term describes curvature-drift acceleration.

In the MHD simulations, the pressure is isotropic so we simply compare the Betatron term $\left(\frac{\partial B}{\partial t} + \mathbf{V}_E \cdot \nabla B\right)$ and the curvature-drift term $(\mathbf{V}_E \cdot \kappa B)$ across different simulations (see Figure 3). This shows that the spatial distribution of the energization mechanisms concurs

with the acceleration regions in section 3.2. Curvature-drift acceleration (right column of Figure 3) is a first-order type Fermi mechanism because reconnecting magnetic fields undergo a net contraction (e.g., Fig. 2c of Dahlin et al. 2017). The Fermi reflection dominates the regions near the X-nullpoints, magnetic islands, and exhausts in the reconnection regions. We note this term is largest at the ends, not the centers, of the two large magnetic islands in Figure 3(c-2). Poor particle trapping in these two islands (particles barely circle around the islands) leads to the weak production of high-energy particles. Betatron acceleration (left column of Figure 3) is also present across different regions and is most important near the solar surface, especially in the turbulent flare loops below the flare CS in Figure 3(b) and 3(e).

3.3.2. *Fluid description of energization mechanisms*

Alternatively, the energy change of magnetized particles could be viewed through the power flow of the magnetic energy,

$$\frac{\partial}{\partial t}\left(\frac{B^2}{8\pi}\right) + \nabla \cdot \mathbf{S} = -\mathbf{E} \cdot \mathbf{J}, \quad (5)$$

where $\mathbf{S} = c\mathbf{E} \times \mathbf{B}/4\pi$ is the Poynting flux (neglecting the displacement current in Ampère's law). The current $\mathbf{J}$ may be split into parallel ($J_\parallel$) and perpendicular components ($\hat{\mathbf{b}} \times (\mathbf{J} \times \hat{\mathbf{b}})$) so it can be rearranged in a form (Dahlin et al. 2016) similar to Eq. (4):

$$\frac{\partial}{\partial t}\left(\frac{B^2}{8\pi}\right) + \nabla \cdot (\frac{B^2}{8\pi}\mathbf{u}_E) = -E_\parallel J_\parallel - \frac{B^2}{8\pi}\nabla \cdot \mathbf{u}_E - (\mathbf{u}_E \cdot \kappa)\frac{B^2}{4\pi} \quad (6)$$

where $\mathbf{u}_E$ and κ are the same variables defined in Eq.(4). The second term on the left-hand side is the divergence of magnetic energy flux, which vanishes in a volume integration. The first term on the RHS ($\mathbf{E}_\parallel \mathbf{J}_\parallel$) is neglected as mentioned above in Eq. (4). The second term on the RHS describes the change in magnetic energy associated with compression or expansion. The third term on the RHS corresponds to the mechanical work done by the magnetic tension force ($\kappa B^2/4\pi$) because it contains the field-line contraction $\mathbf{u}_E \cdot \kappa$ and is therefore related to the Fermi reflection mechanism.

The right column of Figure 4 is similar to the one in Figure 3 due to the fact that they show the Fermi reflection type energy changes (a factor of $|B|/4\pi$ difference). Meanwhile, the spatial distributions of the magnetic field compression and contraction terms in Figure 4 also show similar patterns as the particle energization terms in Figure 3. We also note that in Figure 4(d-1), the compression in the separatrices is releasing energy

to particles while the particles are losing energy through the Betatron term in Figure 3(d-1) for a flare CS with weak guiding field and weak particle acceleration.

For comparison, we examine the maximum amplitudes of the various terms in both Figures. The relative amplitudes of the energization terms in Figure 3 are related as follows: $A_{e,flare} > A_{b,flare} > A_{d,flare} > A_{a,break} > A_{c,break}$, whereas the amplitudes in Figure 4 follow $B_{e,flare} \gg B_{b,flare} \gg B_{d,flare} > B_{a,break} > B_{c,break}$. The orderings are generally consistent with the maximum energy gains in the energy spectra from different reconnecting CSs in Figure 1.

3.4. *Particle distributions*

Due to the nonuniform spatial allocation of different acceleration regions, the distribution of high-energy particles changes significantly throughout the course of the test-particle simulations. At an early time $t = 0.05$ s in the simulation of Figure 1(b), the energy distribution of protons in Figure 5(a) is asymmetric to the midplane.

In another case, in order to compare with the proton trajectories, we simulate the electrons with a similar initial condition to that shown in Figure 1(i). The electrons are well magnetized and mainly move along the magnetic field lines. However, the energetic electrons are ejected to the upper separatrix, which is opposite to the trajectories of energetic protons (Figure 5b). This is consistent with the preferential ejection of oppositely charged particles due to the guiding magnetic field (Zharkova & Gordovskyy 2004; Zharkova & Agapitov 2009).

In Figures 6 and 7, we follow the evolution of the energy distribution of protons in a larger domain $[0.1L_x, 0.9L_x] \times [0.1L_z, 0.9L_z]$, where L_x and L_z stand for the box size of the selected MHD domain ($1R_s \times 0.6R_s$ in the $x - z$ plane). At $t = 0.17$ s, some of the accelerated particles have hit the footpoints and moved to the left boundary of the simulation domain (the bright region at the left edge of Figure 6a). Meanwhile, the ejected antisunward beams move along the separatrix into space. The remaining particles are condensed in the flare loop top region right below the reconnecting X-nullpoint.

Observations during the impulsive phase of solar flares have shown that an external coronal hard X-ray source exists above the thermal loop (Krucker et al. 2008). Here we present the RHESSI image of the X8.2 limb flare SOL2017-09-10 in Figure 6(b), which has been explored extensively in the literature as a flux rope eruption was clearly observed (see Veronig et al. 2018; Yan et al. 2018, for more details). The thermal and nonthermal emissions during the impulsive phase show that,

except for the footpoint nonthermal source at the limb, the contours of different emissions are condensed in the flare. The height of the source increases with the corresponding energy band, as the $100 - 300$ keV hard X-ray (HXR) source is $\approx 5''$ (~ 3.6 Mm) higher than the thermal $6 - 12$ keV source. Similar phenomena have also been reported by the other authors (Masuda et al. 1994; Veronig & Brown 2004; Krucker et al. 2008; Kontar et al. 2011; Oka et al. 2015; Gary et al. 2018). This is consistent with the idea that particles are first accelerated in the reconnecting CS, then ejected to the flare loop (Sui et al. 2004). Although Figure 6(a) only shows the energy distribution of the protons (assuming the two types of charged particles are accelerated in a similar manner), the cusp structure at the apex of the flare loop is in broad agreement with the observed source structure for $30 - 80$ keV.

Later at $t = 0.3$ s in Figure 7(a), the energy distribution peak in the flare loops show that the energetic particles are ejected and move toward the solar surface. Meanwhile, energetic particles are confined and further accelerated near the flare loop top as demonstrated in Figure 2(g), which might explain some examples of prolonged heating (Battaglia et al. 2014; Kuhar et al. 2017). In contrast to other "collapsing magnetic trap" models (Grady et al. 2012; Eradat Oskoui & Neukirch 2014), the flow in the loops is highly turbulent where the Alfvénic reconnection jets interact with the loop top. A related observational study of stochastic turbulence in this region found that there was significant energy in the turbulent plasma motion (Kontar et al. 2017). Determining the conditions required for "collapsing magnetic trap" heating, e.g., at impulsive vs. post-flare phase of the flare requires analysis of the fine-scale time evolution of the MHD simulation, which we leave to a future study.

We show in Figure 7(b) the pitch-angle distribution of high-energy particles, which are highly nonuniform in different regions. Particles ejected from the flare CS are strongly aligned with the local magnetic field lines, while a pancake pitch-angle distribution centered transverse to the magnetic field lines is present in the helmet top region (Lee & Gary 2000; Melnikov et al. 2002) (We note that the highly anisotropic distribution is not isotropized because the large-scale test-particle approach underestimates the instabilities and scattering, etc., which might play an important role in particle transport). This picture is consistent with the discussion in section 3.3.1 that the Fermi reflection primarily accelerates the particles along the magnetic field ($0°$) and the betatron acceleration increases the perpendicular momentum ($90°$) (Northrop 1966; Dahlin et al. 2014; le Roux et al. 2015). A similar study of the pitch angles (not shown here) in

the breakout CS (Figure 1e) shows that the pitch angles are near 0° along the midplane of the chain of the magnetic islands, which indicates the dominant Fermi reflection effects in the midplane near the X-nulls (Xia & Zharkova 2018) (although from Figure 1f we know that the islands there produce comparatively weak particle acceleration).

4. DISCUSSION AND CONCLUSION

We have calculated particle acceleration and transport during CME eruptions occurring via the 'breakout model' (Antiochos 1998). A key point is that the CSs and reconnection all form self-consistently in the MHD simulation due to the slow buildup of the filament channel; hence, the particle acceleration has been calculated for a "realistic" system rather than a preassumed CS. In a breakout eruption, two distinct reconnecting CSs form above and below the erupting CME flux rope and generate many macro-scale X-points and magnetic islands. After the impulsive phase, the guide field of the flare CS decays in agreement with the observed reduction of shear in the magnetic field evolution of eruptive flares (Fletcher et al. 2011). An important issue for all numerical studies of solar activity is the scaling of the results with the grid, i.e., the effective Lundquist number. Since the ARMS code has robust adaptive mesh refinement capabilities, in principle, it is straightforward to perform scaling studies, but one is always limited by the available computational resources, so actual solar Lundquist numbers are far out of reach. In previous 2.5D studies, we have found that beyond a Lundquist number of roughly 1000, or so, the global features of the eruption such as speed, CS length, etc., become essentially independent of refinement level. However, the number of islands in the reconnecting CSs increases dramatically, which is consistent with the predictions of numerous scaling studies (Comisso et al. 2016), and is expected to enhance the particle acceleration efficiency. For the studies of this paper, we simply used the highest resolution MHD simulations presently available to us, and reserve determination of particle acceleration scaling with the numerical resolution to a future paper.

The results presented above lead to a number of important conclusions for both theory and observations. Even though our electromagnetic field model does not include the effects of a parallel electric field, the test-particle simulations demonstrate that particles can be accelerated to high energy ($> 10^8$ eV for protons) in the reconnection CSs in macroscopic systems, and generate a non-Maxwellian tail. Comparisons of energy spectra at different CSs show that particle acceleration is stronger in the flare CS than in the breakout CS.

This is an important result for understanding observations. Breakout reconnection has been observed to produce energetic particles, but these have generally been detected only in radio/microwaves rather than hard X-rays (Maia et al. 2003), indicating that the number of such particles is far smaller than those accelerated in the flare CS. The origin of the difference between the efficiency of flare versus breakout reconnection is in the strength of the electric field $\mathbf{E} = -\mathbf{V} \times \mathbf{B}$ in the two cases. Both the inflow velocity and the magnetic field are much stronger in the flare CS than in the breakout. Furthermore, we find that particle acceleration is stronger during the impulsive phase, consistent with the observation that hard X-ray emission is strongest during the impulsive phase (Dahlin et al. 2017). Again the reason for this is simply in the evolution of the velocity and magnetic fields during the flare reconnection. Initially, the reconnection is driven by the fast ejection of the shear (B_g) field upward to form the escaping flux rope. The reconnection slows down markedly once all the shear has been ejected upwards. The coherent preferential ejection phenomenon due to B_g is also observed in the energy distributions of protons and electrons in our flare CS, which leads to asymmetric spectral signatures of the hard X-ray emission at the two footpoints (Zharkova & Gordovskyy 2004).

By tracing the most energetic particles, we found that acceleration sites include X-nullpoints, magnetic islands, and helmet-like loop tops beneath the flare CS. Another important result is that near the flare CS, a fraction of the energized particles escape antisunward along open magnetic field lines after acceleration. Our results, therefore, can help explain the observed prompt escape of so-called impulsive SEPs. The majority of the energetic particles, however, move sunward after the initial acceleration near the X-nullpoints and in the magnetic islands. Some particles reach the footpoints along the flare loop, as required in order to generate observed hard X-ray sources at the footpoints. Others are captured in the loop top due to the magnetic mirror structure when they are moving downwards, and form the external hard X-ray source in the apex of the flare loop. The trapped particles may be further accelerated in these "collapsing magnetic traps," or may even be re-ejected to the flare CS. We conclude, therefore, that our results are in agreement with many of the classic observations of flare accelerated particles.

Our analysis of the particle transport equation shows that the drift motion of particles along the perpendicular electric field provides strong particle energization. The curvature drift accelerates particles parallel to the magnetic field, and is important in the magnetic islands

and the outflow regions close to the X-nullpoints. In contrast, Betatron acceleration plays an important role further downstream, e.g. at the flare loop top, and preferentially accelerates the particles in the perpendicular direction (also reflected in the pitch-angle distributions). The magnetic energy evolution in the simulation domain suggests that the change of magnetic energy related to flow compression becomes most important in the flare reconnection downstream in the flare loop. The amplitudes of the energization terms in different scenarios are generally consistent with their maximum energy gains of the test particles.

In summary, we have identified particle acceleration processes on large-scale magnetic structures related to explosive CMEs that extend far beyond the small-scale regions where the flux-breaking occurs. The produced energetic particle distribution is not symmetric with respect to the X-nullpoints in the RCSs. Reasons for this behavior include the preferential ejection due to the guiding field B_g, and the magnetic confinement structures, e.g., magnetic islands and helmet-like flare loop tops. These structures could change the transport of energetic particles and even produce a secondary acceleration in the reconnection downstream, or reinject particles into the reconnection CS from the exhaust. The enhancement of hard X-ray emission during the impulsive phase of the flare is due primarily to the highly sheared magnetic field near the polarity inversion line driving explosive guide-field reconnection. Our results suggest that the combined MHD and test-particle simulations could be used to predict the maximum energy gain of particles in different observed magnetic configurations, which may have a critical application to space weather models.

REFERENCES

Amari, T., Luciani, J. F., Mikic, Z., & Linker, J. 2000, ApJL, 529, L49

Andrews, M. 2003, Solar Physics, 218, 261

Antiochos, S. K. 1998, ApJL, 502, L181

Antiochos, S. K., Dahlburg, R. B., & Klimchuk, J. A. 1994, ApJL, 420, L41

Antiochos, S. K., DeVore, C. R., & Klimchuk, J. A. 1999, The Astrophysical Journal, 510, 485

Battaglia, M., Fletcher, L., & Simões, P. J. A. 2014, ApJ, 789, 47

Birn, J., Battaglia, M., Fletcher, L., Hesse, M., & Neukirch, T. 2017, The Astrophysical Journal, 848, 116

Boris, J. P. 1970, Proceeding of Fourth Conference on Numerical Simulations of Plasmas

Borissov, A., Neukirch, T., & Threlfall, J. 2016, SoPh, 291, 1385

Borissov, A., Kontar, E. P., Threlfall, J., & Neukirch, T. 2017, A&A, 605, A73

Comisso, L., Lingam, M., Huang, Y. M., & Bhattacharjee, A. 2016, Physics of Plasmas, 23, 100702

Dahlin, J. T., Antiochos, S. K., & DeVore, C. R. 2019, ApJ, 879, 96

Dahlin, J. T., Drake, J. F., & Swisdak, M. 2014, Physics of Plasmas, 21, 092304

—. 2016, Physics of Plasmas, 23, 120704

Dahlin, J. T., Drake, J. F., & Swisdak, M. 2017, Physics of Plasmas, 24, 092110

Daughton, W., Roytershteyn, V., Karimabadi, H., et al. 2011, Nature Physics, 7, 539

DeVore, C. R., & Antiochos, S. K. 2008, ApJ, 680, 740

Drake, J. F., Arnold, H., Swisdak, M., & Dahlin, J. T. 2019, Physics of Plasmas, 26, 012901

Drake, J. F., Cassak, P. A., Shay, M. A., Swisdak, M., & Quataert, E. 2009a, Ap. J., 700, L16

Drake, J. F., Shay, M. A., Thongthai, W., & Swisdak, M. 2005, Physical Review Letters, 94, 095001

Drake, J. F., Swisdak, M., Che, H., & Shay, M. A. 2006, Nature, 443, 553

Drake, J. F., Swisdak, M., Phan, T. D., et al. 2009b, J. Geophys. Res., 114, doi:10.1029/2008JA013701

Egedal, J., Daughton, W., & Le, A. 2012, Nature Physics, 8, 321

Emslie, A. G., Dennis, B. R., Holman, G. D., & Hudson, H. S. 2005, Journal of Geophysical Research (Space Physics), 110, A11103

Emslie, A. G., Dennis, B. R., Shih, A. Y., et al. 2012, ApJ, 759, 71

Eradat Oskoui, S., & Neukirch, T. 2014, A&A, 567, A131

Fan, Y. 2010, ApJ, 719, 728

Fletcher, L., Dennis, B. R., Hudson, H. S., et al. 2011, Space Science Reviews, 159, 19

Forbes, T. G., Linker, J. A., Chen, J., et al. 2006, SSRv, 123, 251

Gaizauskas, V. 1998, in Astronomical Society of the Pacific Conference Series, Vol. 150, IAU Colloq. 167: New Perspectives on Solar Prominences, ed. D. F. Webb, B. Schmieder, & D. M. Rust, 257

Gary, D. E., Chen, B., Dennis, B. R., et al. 2018, The Astrophysical Journal, 863, 83

Gordovskyy, M., & Browning, P. K. 2012, SoPh, 277, 299

Gordovskyy, M., Browning, P. K., & Vekstein, G. E. 2010a, A&A, 519, A21

—. 2010b, ApJ, 720, 1603

Gosling, J. T. 1993, Journal of Geophysical Research: Space Physics, 98, 18937

Gosling, J. T. 1994, J. Geophys. Res., 99, 4259

Grady, K. J., Neukirch, T., & Giuliani, P. 2012, A&A, 546, A85

Guo, F., Li, H., Daughton, W., & Liu, Y.-H. 2014, Physical Review Letters, 113, 155005

Hockney, R. W., & Eastwood, J. W. 1981, Computer Simulation Using Particles (New York: McGraw-Hill)

Holman, G. D., Aschwanden, M. J., Aurass, H., et al. 2011, SSRv, 159, 107

Hudson, H., Haisch, B., & Strong, K. T. 1995, J. Geophys. Res., 100, 3473

Isliker, H., Archontis, V., & Vlahos, L. 2019, ApJ, 882, 57

Karlický, M., & Bárta, M. 2006, ApJ, 647, 1472

—. 2007, Advances in Space Research, 39, 1427

Karpen, J. T., Antiochos, S. K., & DeVore, C. R. 2012, The Astrophysical Journal, 760, 81

Kay, H. R. M., Harra, L. K., Matthews, S. A., Culhane, J. L., & Green, L. M. 2003, A&A, 400, 779

Knizhnik, K., Swisdak, M., & Drake, J. F. 2011, ApJL, 743, L35

Kontar, E. P., Perez, J. E., Harra, L. K., et al. 2017, Phys. Rev. Lett., 118, 155101

Kontar, E. P., Brown, J. C., Emslie, A. G., et al. 2011, Space Science Reviews, 159, 301

Krucker, S., Battaglia, M., Cargill, P. J., et al. 2008, A&A Rv, 16, 155

Kuhar, M., Krucker, S., Hannah, I. G., et al. 2017, ApJ, 835, 6

le Roux, J. A., Zank, G. P., Webb, G. M., & Khabarova, O. 2015, ApJ, 801, 112

Lee, J., & Gary, D. E. 2000, ApJ, 543, 457

Li, X., Guo, F., Li, H., & Birn, J. 2018, The Astrophysical Journal, 855, 80

Lin, R., & Team, R. 2003, Advances in Space Research, 32, 1001 , connections and Reconnections in Solar and Stellar Coronae

Lin, R. P., & Hudson, H. S. 1976, SoPh, 50, 153

Maia, D., Aulanier, G., Wang, S. J., et al. 2003, A&A, 405, 313

Martin, S. F. 1998, SoPh, 182, 107

Masuda, S., Kosugi, T., Hara, H., Tsuneta, S., & Ogawara, Y. 1994, Nature, 371, 495

Melnikov, V. F., Shibasaki, K., & Reznikova, V. E. 2002, ApJL, 580, L185

Miller, J. A., Cargill, P. J., Emslie, A. G., et al. 1997, J. Geophys. Res., 102, 14631

Montag, P., Egedal, J., Lichko, E., & Wetherton, B. 2017, Physics of Plasmas, 24, 062906

Moore, R. L., Sterling, A. C., Hudson, H. S., & Lemen, J. R. 2001, ApJ, 552, 833

Nalewajko, K., Uzdensky, D. A., Cerutti, B., Werner, G. R., & Begelman, M. C. 2015, The Astrophysical Journal, 815, 101

Northrop, T. G. 1966, in Radiation Trapped in the Earth's Magnetic Field, ed. B. M. McCormac (Dordrecht: Springer Netherlands), 26–44

Oka, M., Krucker, S., Hudson, H. S., & Saint-Hilaire, P. 2015, ApJ, 799, 129

Oka, M., Phan, T.-D., Krucker, S., Fujimoto, M., & Shinohara, I. 2010, ApJ, 714, 915

Priest, E., & Forbes, T. 2000, Magnetic Reconnection (Cambridge University Press), 612

Ripperda, B., Bacchini, F., Teunissen, J., et al. 2018, The Astrophysical Journal Supplement Series, 235, 21

Siversky, T. V., & Zharkova, V. V. 2009, Journal of Plasma Physics, 75, 619

Somov, B. V., & Kosugi, T. 1997, ApJ, 485, 859

Somov, B. V., & Oreshina, A. V. 2000, A&A, 354, 703

Speiser, T. W. 1965, J. Geophys. Res., 70, 4219

Sui, L., Holman, G. D., & Dennis, B. R. 2004, ApJ, 612, 546

Titov, V. S., Mikic, Z., Linker, J. A., & Lionello, R. 2008, The Astrophysical Journal, 675, 1614

Turkmani, R., Cargill, P. J., Galsgaard, K., Vlahos, L., & Isliker, H. 2006, A&A, 449, 749

Veronig, A. M., & Brown, J. C. 2004, The Astrophysical Journal, 603, L117

Veronig, A. M., Podladchikova, T., Dissauer, K., et al. 2018, The Astrophysical Journal, 868, 107

Vilmer, N. 2012, Philosophical Transactions of the Royal Society A: Mathematical, Physical and Engineering Sciences, 370, 3241

Vilmer, N., MacKinnon, A. L., & Hurford, G. J. 2011, SSRv, 159, 167

Wyper, P. F., Antiochos, S. K., & DeVore, C. R. 2017, Nature, 544, 452

Xia, Q., & Zharkova, V. 2018, A&A, 620, A121

Yan, X. L., Yang, L. H., Xue, Z. K., et al. 2018, The Astrophysical Journal, 853, L18

Zank, G. P., le Roux, J. A., Webb, G. M., Dosch, A., & Khabarova, O. 2014, ApJ, 797, 28

Zharkova, V. V., & Agapitov, O. V. 2009, Journal of Plasma Physics, 75, 159

Zharkova, V. V., & Gordovskyy, M. 2004, ApJ, 604, 884

Zharkova, V. V., Arzner, K., Benz, A. O., et al. 2011, SSRv, 159, 357

Zhou, X., Bchner, J., Bárta, M., Gan, W., & Liu, S. 2016, The Astrophysical Journal, 827, 94
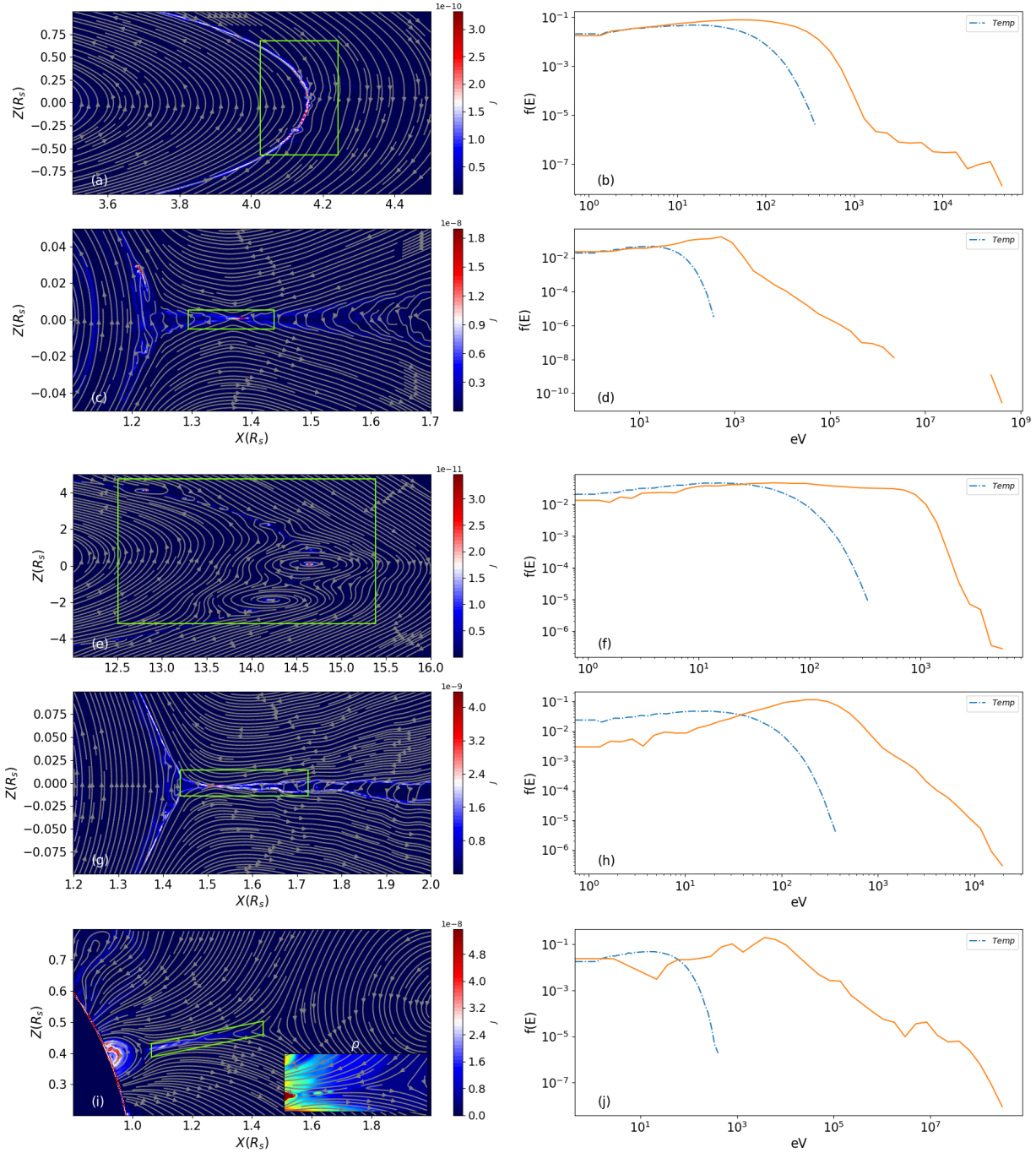
Figure 1. The left column contains the current densities in five different MHD simulation regions (the in-plane magnetic field lines are in gray; the green boxes indicate where the test particles are initialized). The right column shows the corresponding energy spectra of protons at the end of the simulations (blue dashed-dotted lines benchmark the initial status). From top to bottom: (a) the breakout CS and (c) flare CS from the same 2.5D MHD simulation with a strong guiding field; (e) the breakout CS and (g) flare CS from another 2.5D simulation with a weak guiding field; (i) the flare CS in the plane of a 3D simulation with a strong guiding field, in which the plasma density distribution shows the magnetic islands in the CS more clearly at the right corner.
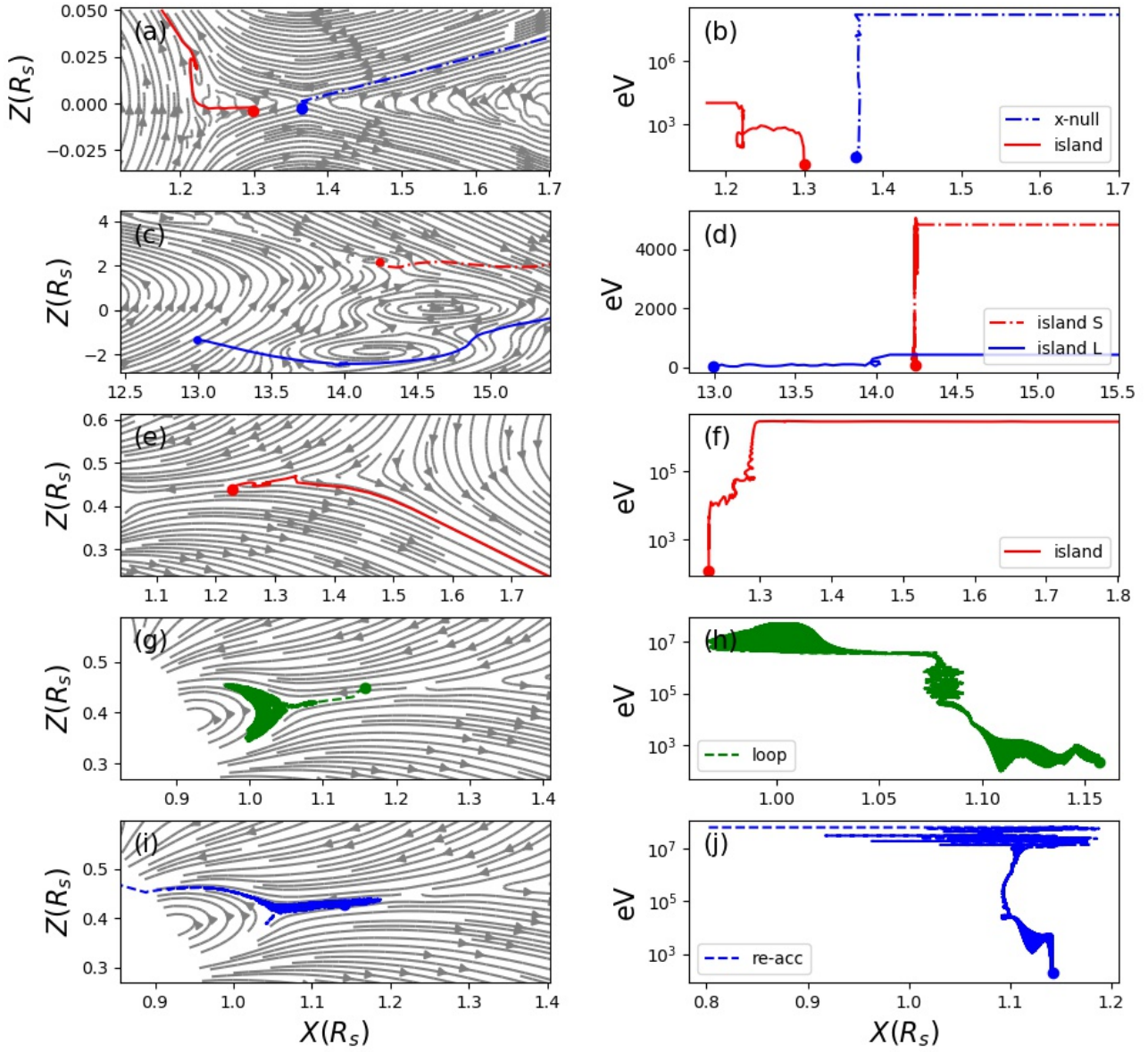
Figure 2. The left column shows the trajectories of energetic particles in the magnetic fields. The corresponding particle energy versus their $x-$coordinates are arranged in the right column.
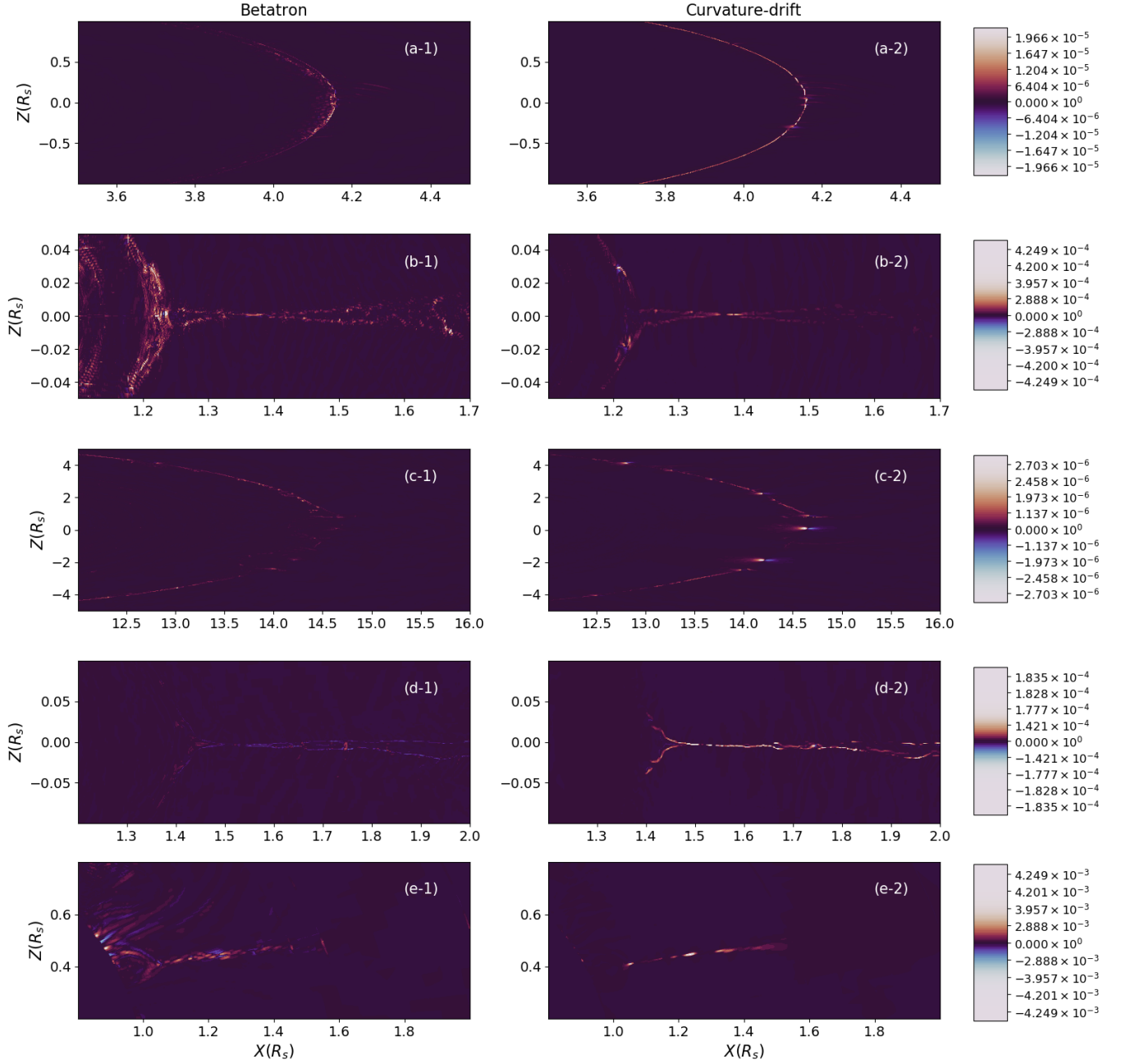
Figure 3. Left sequence shows the distributions of the second term in Eq. (4) for different cases in Figure 1. The right sequence shows the distributions of the third term of Eq. (4).
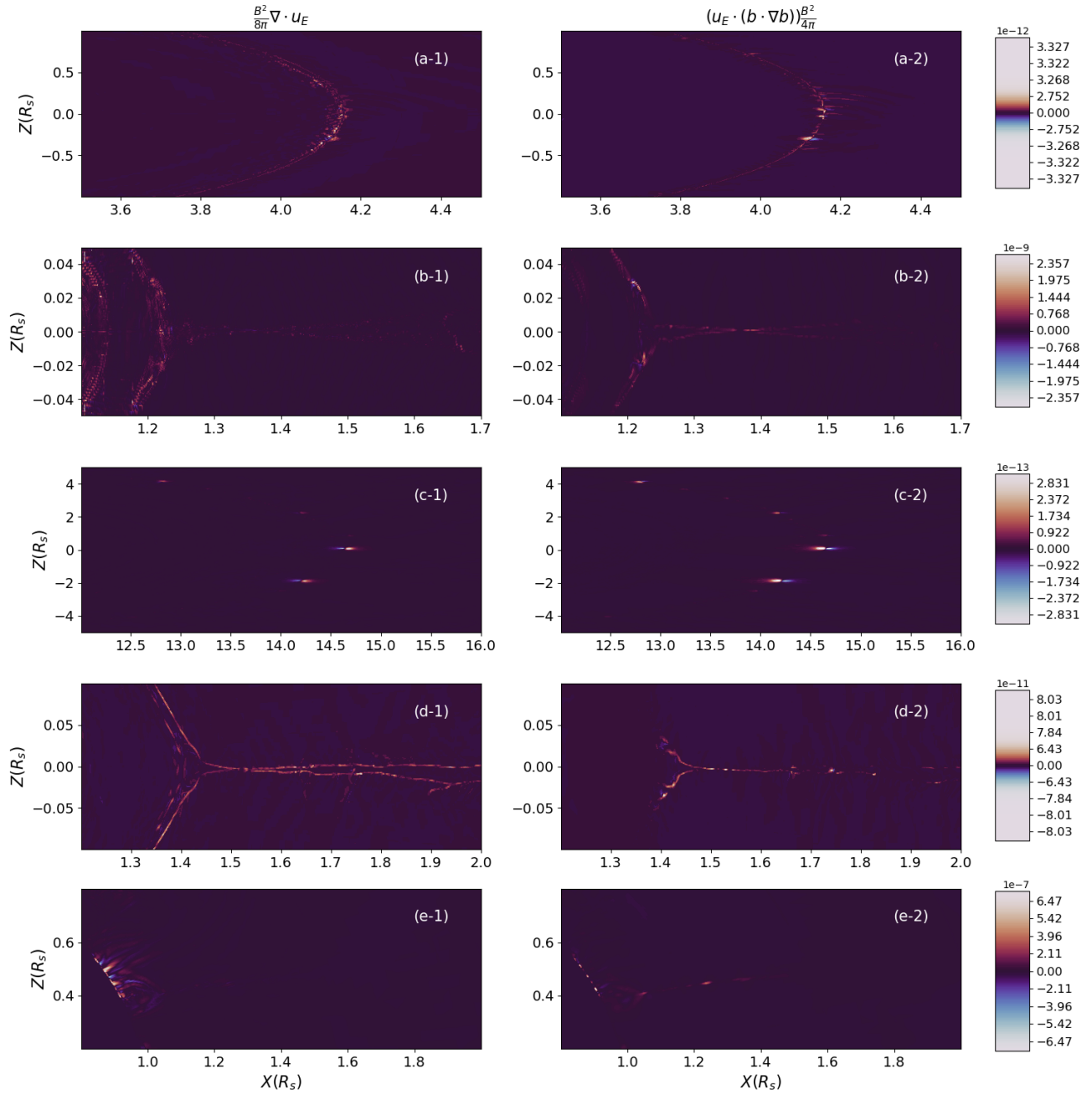
Figure 4. The left column shows the distributions of the compression term in Eq. (6) for different cases in Figure 1. The right column shows the distributions of the field-line contraction terms.
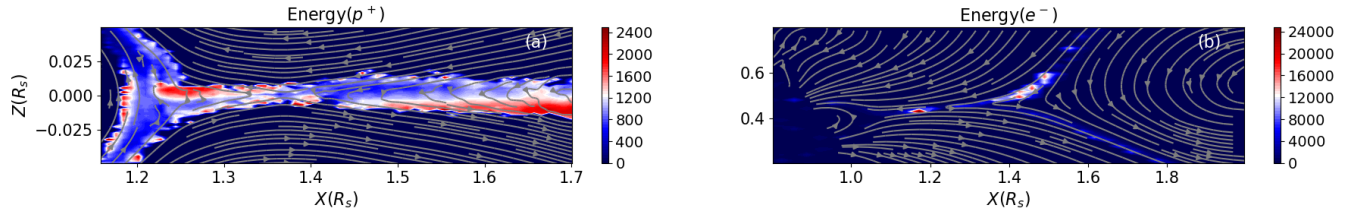
Figure 5. The left panel shows the energy distribution of protons in the simulation of Figure 1(b) at $t = 0.05$ s. The energy distribution of electrons on the right comes from the simulation of Figure 1(i) at $t = 1.0 \times 10^{-4}$ s.
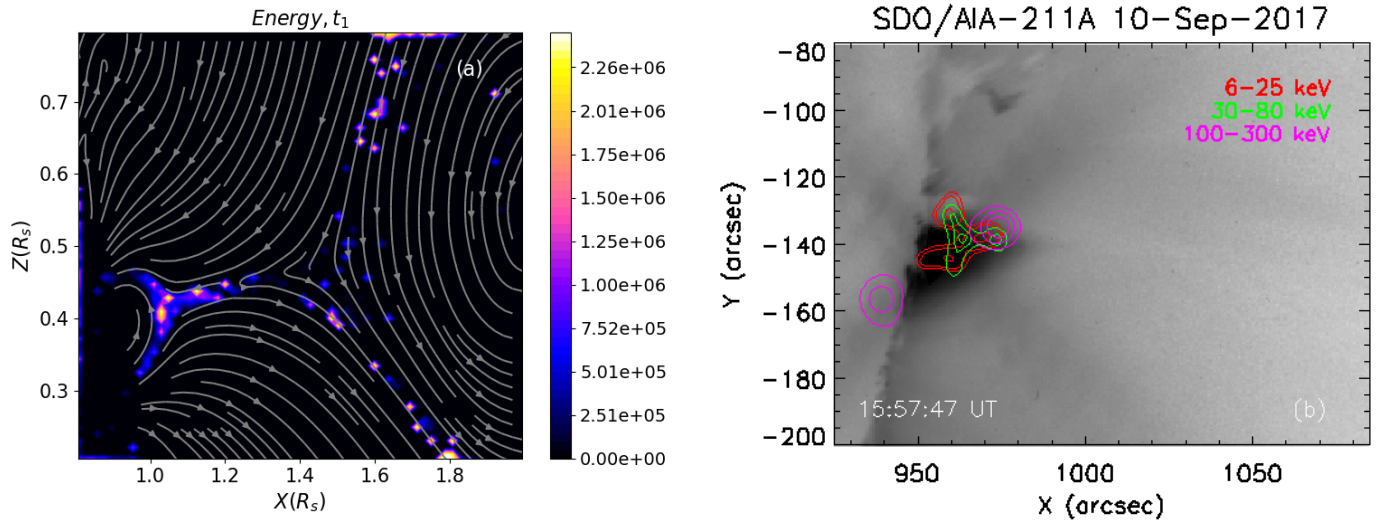

Figure 6. (a) Energy distribution of particles at $t = 0.17$ s, and (b) Imaging of the 2017 September 10 flare. The emission at $6 - 25$ keV, $30 - 80$ keV, and $100 - 300$ keV are shown in red, green, and pink contours plotted on a SDO/AIA $211\mathring{A}$ image taken at $15:57:47$ UT. The $RHESSI$ HXR images are reconstructed using the PIXON algorithm and the shown contour levels are 40%, 70%, and 90%.
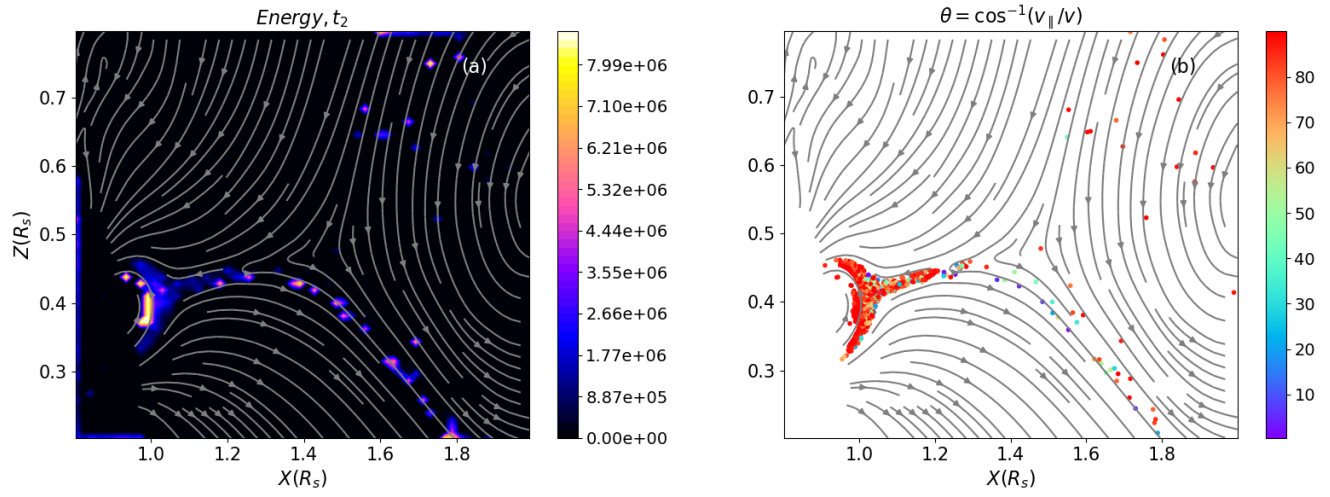
Figure 7. (a) Energy distribution of particles at $t = 0.3$ s after Figure 6, and (b) the corresponding pitch-angle distribution of high-energy particles ($> 10^6$ eV) of (a).